HHS Public Access

Author manuscript

Environ Sci Technol. Author manuscript; available in PMC 2021 March 11.

Published in final edited form as:

Environ Sci Technol. 2020 November 17; 54(22): 14716–14724. doi:10.1021/acs.est.0c04645.

Effect of Nonphosphorus Corrosion Inhibitors on Biofilm Pore Structure and Mechanical Properties

Conghui Huang,
Department of Civil and Environmental Engineering, University of Illinois at Urbana-Champaign, Urbana, Illinois 61801, United States

Peter P. Sun,
Department of Civil and Environmental Engineering, University of Illinois at Urbana-Champaign, Urbana, Illinois 61801, United States

Jungeun Won,
Departments of Electrical and Computer Engineering and Bioengineering, Beckman Institute for Advanced Science and Technology, University of Illinois at Urbana-Champaign, Urbana, Illinois 61801, United States

Yin Wang,
Department of Civil and Environmental Engineering, University of Wisconsin—Milwaukee, Milwaukee, Wisconsin 53201, United States

Stephen A. Boppart,
Departments of Electrical and Computer Engineering and Bioengineering, Beckman Institute for Advanced Science and Technology and Carle Illinois College of Medicine, University of Illinois at Urbana-Champaign, Urbana, Illinois 61801, United States

Thanh H. Nguyen
Department of Civil and Environmental Engineering, Institute of Genomic Biology, and Carle Illinois College of Medicine, University of Illinois at Urbana-Champaign, Urbana, Illinois 61801, United States

Abstract

Understanding the effects of biofilm structural and mechanical properties, which can influence biofilm cohesiveness and detachment under physical stress, is critical for biofilm and biofilm-associated pathogen control. In this study, we used optical coherence tomography (OCT) and nanoindentation to determine the role of silicate and tin (two experimental nonphosphate corrosion inhibitors) on the porous structure and stiffness of three types of multispecies biofilms. These

Corresponding Author Thanh H. Nguyen – Department of Civil and Environmental Engineering, Institute of Genomic Biology, and Carle Illinois College of Medicine, University of Illinois at Urbana-Champaign, Urbana, Illinois 61801, United States; thn@illinois.edu.

Supporting Information

The Supporting Information is available free of charge at https://pubs.acs.org/doi/10.1021/acs.est.0c04645.

Additional information regarding confirming the presence of bacteria in these biofilms, the representative force–indentation curves, the image analysis workflow, and the biofilm 3D reconstruction images (PDF)

The authors declare no competing financial interest.

biofilms were grown from groundwater (a drinking water source), and this groundwater was amended with either tin or silicate corrosion inhibitor (0.5 mg/L as Sn and 20 mg/L as SiO_2). Based on the elastic moduli of these biofilms, tin biofilms and groundwater biofilms were the stiffest, followed by silicate biofilms. The thickness normalized by the growth time for silicate biofilms was highest at 38 ± 7.1 μm/month, compared to 21 ± 3.2 and 11 ± 2.4 μm/month for tin biofilms and groundwater biofilms, respectively. The silicate biofilms had the greatest overall porosities and were thickest among the three biofilms. Based on the pore network modeling (PNM) of OCT images, larger pores and connections were found in the silicate biofilms compared to those in tin and groundwater biofilms. Our analysis showed that the thicker and more porous biofilms (silicate biofilms) were potentially less resistant to deformation than the thinner and denser biofilms (tin and groundwater biofilms).

Graphical abstract

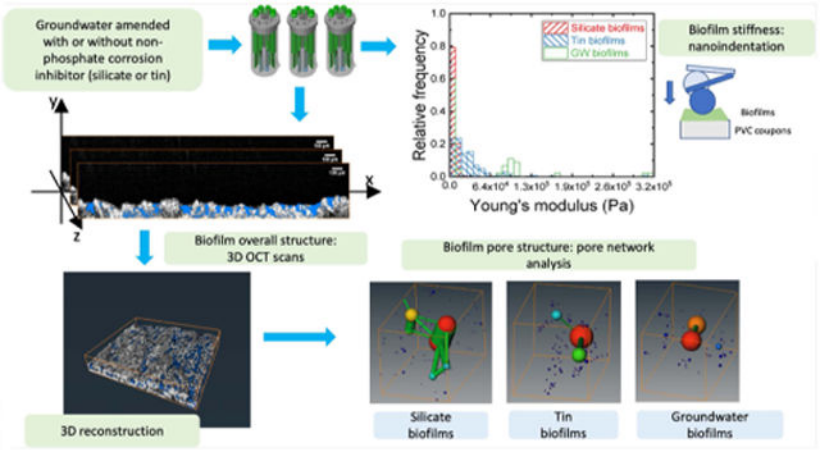

INTRODUCTION

Biofilms, a porous matrix developed by microorganisms accumulating on a surface, are ubiquitous in drinking water distribution systems (DWDS).[1-5] They also play an important role in opportunistic pathogen survival and propagation in both large-scale DWDS and small-scale premise plumbing systems.[6] About 60% of infections by *Legionella*, an opportunistic pathogen commonly found in premise plumbing, was attributed to the lack of disinfectants, which can be depleted during contact with the biofilm matrix.[7] The presence of biofilms in DWDS can also cause color and taste problems in the drinking water.[2] Multiple factors in the distribution systems contribute to biofilm growth in drinking water. Hydrodynamic conditions, such as pressure changes induced by the daily water use pattern and stagnation zone at the end of the distribution systems, can play a role in biofilm release and development on the pipe surfaces. Water quality characteristics such as organic matter and disinfectants were used to control biofilms or microorganism regrowth in drinking water.[8-10] Corrosion inhibitors, which are commonly added into drinking water due to aging DWDS to reduce lead and copper levels in drinking water, are usually phosphate-based and can provide nutrients to microorganisms grown inside the premise plumbing systems.[11] The application of nonphosphate corrosion inhibitors can be a potential alternative to balance the

goals between corrosion control and microbial regrowth in DWDS. Nonphosphate corrosion inhibitors such as silicate and tin were reported to reduce the soluble metal (lead, copper, and zinc) leaching from the distribution system pipes by increasing the pH or forming protective layers on the inner pipe surface.[12-15] However, few studies have characterized the biofilm growth under the influence of these corrosion inhibitors.

Knowledge of the pore structure and stiffness of the biofilm matrix is important to understand the effect of the nonphosphate corrosion inhibitors on biofilm growth and release. Previously, the overall biofilm structure (thickness, roughness, porosity, etc.) and development were characterized and monitored by noninvasive imaging techniques such as optical coherence tomography (OCT).[16-20] The pore structure of the biofilms, usually filled with water, can control the transport of nutrients and antimicrobial substances into the biofilm matrix, which is composed of cells and extracellular polymeric substances (EPS).[21,22] The spatial distributions of cells and EPS have been characterized by confocal laser scanning microscopy (CLSM) and OCT.[20,23] However, few studies have determined the spatial pore structure. Under shear stress of the water flow, more biofilms and pathogens can be released from biofilms with lower stiffness compared to biofilms with higher stiffness.[24-27] However, due to factors such as chemical composition in the feeding water, biofilm age, microbial community structure, and hydrodynamic conditions, a wide range of stiffness ($10–10^8$ Pa) has been reported.[28-31] This wide range of stiffness implied that biofilms grown under different conditions could demonstrate different resistance when biofilms were exposed to shear stress. Biofilms can also adapt to increasing shear stress by shifting the microbial community structure and EPS composition.[32] Although studies showed that the relative porosity could impact the mechanical properties of implants in bone tissue engineering,[33-35] the role of the chemical composition in the feeding water on the biofilm pore structure and stiffness has not been studied. Better control of biomass and pathogens released from biofilms requires an understanding of the biofilm properties developed in drinking water-relevant conditions.

The study objective was to fill the knowledge gap on the effect of nonphosphate corrosion inhibitors on biofilm porous structure and stiffness and the linkage between these biofilm properties. Silicate (sodium metasilicate) and tin (tin sulfate) were chosen to represent a common and experimental nonphosphate corrosion inhibitor, respectively. Groundwater biofilms without corrosion inhibitors were used as the control. In this study, we (1) characterized the entire structure of bulk biofilms by OCT, a technique that does not require staining; (2) determined biofilm stiffness by nanoindentation; and (3) characterized the spatial pore structure of these biofilms by pore network analysis using Avizo (Thermo Fisher Scientific). This is the first study showing that the amendment of nonphosphate corrosion inhibitors led to biofilms with different pore structure and stiffness. Specifically, a more porous biofilm was formed under the influence of silicate corrosion inhibitor compared to that of tin.

METHODS

Biofilm Growing Conditions.

Biofilms were grown on the cylindrical poly(vinyl chloride) (PVC) coupons (12.7 mm in diameter, RD 128-PVC, BioSurface Technologies Corporation, Bozeman, MT), a common material in premise plumbing, in three CDC reactors (CBR 90-2, BioSurface Technologies Corporation). These reactors were fed by groundwater, the drinking water source in Urbana-Champaign, IL, after passing through a greensand filter to remove iron and manganese precipitates, similar to filtration at the local drinking water treatment plant. This groundwater was pumped from a well underneath the Newmark Civil Engineering Lab (Urbana, IL) without disinfection treatment. Two nonphosphate corrosion inhibitors, tin (0.5 mg/L as Sn) and silicate (20 mg/L as SiO_2), were chosen to simulate experimental and common alternatives in drinking water, respectively.[12,14] Their concentrations were selected based on those reported in practical applications and lab/pilot-scale investigations.[12-14,36] The groundwater-containing silicate was prepared by adding Na_2SiO_3 (Sigma-Aldrich) to 10 L of groundwater to reach a final concentration of 20 mg/L as SiO_2. $SnSO_4$ (Sigma-Aldrich) was added to 10 L of groundwater to reach a final concentration of 0.5 mg/L as Sn. The groundwater with or without a corrosion inhibitor was prepared freshly every 2 or 3 days. The CDC reactors were maintained at 125 rpm (Re = 3510) to simulate the shear stress presented in the DWDS. The feeding groundwater was pumped into the reactors at a flow rate of 1.3 mL/min. The biofilms fed by the groundwater amended with two corrosion inhibitors were grown for 6 months. The biofilms fed by groundwater were grown for 12 months to allow sufficient biofilm development for nanoindentations. The presence of the bacteria in these biofilms was confirmed by DNA extraction and quantitative polymerase chain reaction (qPCR), as described in the Supporting Information.

Nanoindentation on Biofilms Developed with Groundwater with or without Two Corrosion Inhibitors.

The stiffness of the biofilms fed by groundwater with or without two corrosion inhibitors was determined using a Piuma nanoindenter (Optics11, Amsterdam, the Netherlands). The stiffness was represented by Young's modulus, which represented the deformation of biofilms under physical stress. The greater the Young's modulus, the greater resistance the material had to the deformation under the stress extended by fluid flow. Two to three coupons were taken from each reactor and fixed to the bottom of a 35 mm diameter Petri dish by superglue. A precalibrated glass probe with a radius of 23.5 or 32.5 μm and a cantilever with stiffness ranging from 0.434 to 0.48 N/m was indented into the biofilms with a maximum limit of cantilever extension of 10 μm. The difference in tip radii was corrected in the calculation of the elastic modulus for the biofilms, as shown in eq 1. All indentations were carried out on biofilm-covered coupons submerged in the same groundwater condition that was used to grow these biofilms. The probe was calibrated in the biofilm feeding water (groundwater and groundwater-containing silicate or tin) on a clean bottom of the Petri dish before each indentation experiment, following the instrument instructions. The probe was allowed to indent onto the bottom of the Petri dish, and the voltage change induced by the bending of the cantilever was monitored and used as a threshold for the detection of biofilm surface. If the voltage change was below this threshold, the cantilever was considered to be

not bending. This means that if we probe the pores that were filled with water and opened to the surface, the voltage change will be lower than the threshold. The relationship between force and indentation by the probe was measured and recorded by the instrument software, as shown in Figure S1. Six to thirteen locations were randomly chosen on each coupon from each type of biofilm and indented with the probe. A series of approaching velocities of 0.5, 1, 2, or 5 μm/s were used in the indentation profile to access the viscoelasticity of the biofilm stiffness. Indentations were repeated 2–3 times with the same indentation profile at each location. The contamination of the probe was checked by indenting on a clean Petri dish bottom, and the results were compared with the force–distance curves obtained from the calibration of the clean probe. The contaminated probe was washed with isopropanol and water, as instructed by the manufacturer. The distributions of the elastic moduli of these three biofilms were obtained by fitting the force–indentation curves with the Hertz model (eq 1),[37] one of the most common methods to model the nanoindentation experiment with a small range of indentations (less than 10% compared to the sample thickness)[38-40]

$$F = \frac{4 \times (1 - \upsilon)}{3 \times E} \times (R \times d^3)^{1/2} \quad (1)$$

where F is the contact force, R is the tip radius, d is the indentation, υ is Poisson's ratio and assumed to be 0.5 (soft material), and E is the elastic modulus. Due to the assumption of shallow indentation (10% of sample thickness) in Hertz's model, the average biofilm thickness should be greater than 10% of the indentation depth.[41] For this reason, we only subjected biofilms with thickness greater than 90 μm to nanoindentation. We monitored the thickness of the biofilms over the growing period and found that 12 months were necessary to obtain biofilm thick enough for nanoindentation.

OCT Imaging and Overall Biofilm Characterization.

Three coupons were taken out from each reactor for optical coherence tomography (OCT) imaging with a scan dimension of 3.13 mm × 4.18 mm × 4 mm. Three randomly chosen locations from each coupon were imaged. For each location, 200 images were taken. Three randomly chosen locations from each coupon were imaged by a custom-built spectral-domain optical coherence tomography (SD-OCT). A superluminescent diode source with a center wavelength and bandwidth of 1310 ± 85 nm (LS2000B, Thorlabs) was used with a 1024-pixel InGaAs line-scan camera (SU-LDH2, Goodrich) for detection and a two-dimensional (2D) galvanometer scanner (GVS102, Thorlabs) for scanning. The achromatic lens (f = 50 mm, Thorlabs) was used as the objective lens. The system was operated at an ~92 kHz line-scan rate and had a resolution of ~8 and ~20 μm in axial and transverse directions, respectively. More details on OCT system can be found from an earlier publication.[42] The cross-sectional biofilm images were preprocessed for orientation corrections using Fiji version 2.00.[43] Approximately 100–180 frames in the middle of the stack were selected for the overall biofilm structural characterization (eq 2). In total, over 2000 images were analyzed. The orientation of image stacks was corrected manually by transformation and rotation. The PVC surface in each frame was aligned to the same height along with the scanning direction in the same stack. The coordinates of the PVC surface were determined based on the first frame in each stack. The overall biofilm surface was extracted by the default auto thresholding using a modified version of the IsoData algorithm

by iteratively increasing the threshold to above the composite average of the pixels in the background (at or below threshold) and in the biofilm surface (above threshold). The local biofilm thickness (optical thickness) was determined by subtracting the height of the marked PVC surface from the height of the identified biofilm surface for each cross-sectional image using MATLAB codes, as described previously.[17,44] The refractive indices of 1.33–1.38 were obtained from three biofilms. The physical biofilm thickness was obtained by dividing the optical thickness by the corresponding refractive index

$$z(\text{mean}) = \frac{1}{n} \times \sum z_i \tag{2}$$

where z was the local biofilm thickness along the horizontal direction in each OCT frame and n is the number of thickness measurements along the horizontal direction. The normalized thickness of three biofilms was calculated by normalizing the mean biofilm thickness by the growth period of the corresponding biofilms.

Biofilm Three-Dimensional (3D) Reconstruction and Pore Structure Analysis.

We followed the image processing methods used by previous studies, which reconstructed 3D images obtained from porous materials such as rock and soil samples.[45,46] We analyzed five to six locations on each biofilm type. For each imaging location, about 100–180 sequential images in the middle of the stack, which had consistent image quality, were selected for biofilm reconstruction and pore structure analysis. Figure S2 is representative rendering images obtained from the 3D reconstruction of these OCT image stacks of the tin biofilm. These rendering images were further analyzed to quantify the biofilm porous structure, including the overall porosities, and the pore network model using Avizo. The biofilm matrices containing both biomass and pore space were created from five randomly chosen images among 100–180 images that were obtained along the scanning direction for each OCT stack (one image was selected from every 20–30 images). These biofilm matrices were used to filter out the air-filled space above biofilms. The image analysis included six steps, as described in the flow diagram in Figure S3. In step 1, the nonorthogonal angle shift introduced during the OCT image collection to reduce water deflection was corrected for the collected images using the Shear module in Avizo. In step 2, the intensity of image slices was adjusted by normalizing the background intensity. In step 3, the images were smoothed and denoised by the Despeckle module. In step 4, the pixel intensity of zero was recognized as the pore space in an image frame using the “Top-hat” function every 280–380 μm (15–20 frames) apart from the processed stack with 1980–3580 μm (100–180 frames) depending on the image quality. The results of step 4 could include the pore space outside of the biofilm, and this pore space needed to be removed in steps 5 and 6. In step 5, the biofilm volume was extracted from the whole matrix by automatic thresholding and adjusted by a “fill-hole” function. Artificial elements created in this step were removed by the 3D erosion module. In step 6, the pores outside the biofilm were removed by subtracting the simulated 3D images created in step 5 from those in step 4. The pores were identified in voxels with an intensity of zero, while the biomass was identified in voxels with nonzero intensity values, as shown in Figures S2 and S4. Over 2000 images were analyzed for these three biofilms.

The overall porosity of the biofilms was determined by the ratio between the pore and biofilm volume. The pore structure models were constructed based on the connected pores obtained from step 6 using a pore network analysis module in Avizo. The pore volume for each biofilm pore space was characterized by a network generated by a series of theoretically spherical pores connected by cylindrical throats. These pore networks characterized the spatial pore structure developed under groundwater with or without nonphosphate corrosion inhibitors. The total number of pores and connected throats normalized by the biofilm matrix volume obtained from step 5 and the distributions of pore size and throat length were reported and analyzed. Two pore network analyses were applied to the pore space isolated from each OCT scanned location of two coupons taken from these reactors.

Statistical Analysis.

Statistical comparisons were performed by the nonparametric Kolmogorov–Smirnov (KS) test and the Wilcoxon rank-sum test using R (version 3.6.2). A bootstrap version of the Kolmogorov–Smirnov test was used when the distributions contained ties.[47] Percentiles and medians of the data set were obtained from R. A significant difference was determined by the p-value lower than 0.05.

RESULTS

Softest Silicate Biofilms Compared to Tin and Groundwater Biofilms.

The effect of time-dependent force on biofilm stiffness was determined by plotting the distributions of elastic moduli over four approaching velocities (Figure 1). For all biofilms, the measured stiffness did not significantly change with the approaching velocity (KS test, $p > 0.05$). The 1 year biofilms grown without corrosion inhibitors had a median elastic modulus ranging from 7.5 to 8.9 kPa measured with 0.5–2 μm/s approaching velocities. The 10th and 90th percentiles of these groundwater biofilms were 1.4 and 165 kPa, respectively. This range of approaching velocity was chosen because biofilm stiffness obtained from the silicate and tin biofilms did not significantly change under the approaching velocity ranging from 0.5 to 5 μm/s. Note that the indentation was in the range of 3–7 μm deep into the biofilm surface. This thickness is less than 10% of the overall thickness of the biofilm. Therefore, the stiffness measurement was not influenced by the PVC coupons, on which the biofilms were grown. Because the difference in elastic moduli obtained with the approaching velocities in the range of 0.5–5 μm/s was not detected, all three biofilms demonstrated elastic rather than viscoelastic behavior in this range of approaching velocity. In contrast to this observation, single-species biofilms, which were usually cultured within days (instead of over 6 months for tin and silicate biofilms or 12 months for groundwater biofilms), demonstrated more apparent viscous properties than elastic properties at higher frequencies, [48] while elastic properties dominated using indentation at low approaching velocity range.[30]

We also compared the distribution of elastic moduli obtained from 0.5 to 2 μm/s for the three types of biofilms, as shown in Figure 2. The distribution of elastic moduli for these three biofilms was approximated by the log–normal functions. Tin biofilms have a significantly greater stiffness than both groundwater and silicate biofilms (KS test, $p < 0.05$). The median

elastic modulus observed from tin biofilms was 19 kPa with 10th and 90th percentiles at 5.9 and 57 kPa, while the median elastic modulus obtained from silicate biofilms was 4.8 kPa with 10th and 90th percentiles at 1.7 and 12 kPa, respectively. The median elastic modulus obtained from groundwater biofilms was 7.5 kPa with 10th and 90th percentiles at 1.4 and 165 kPa, respectively. Previous studies suggested that stiffer biofilms can be more resistant to biomass release by physical stress.[24,26] Among the three studied biofilms, the tin biofilms were the most resistant to deformation and subsequent detachment. Compared with silicate biofilms, groundwater biofilm was likely to resist deformation and detachment.

Thicker and Most Porous Biofilms Developed under Groundwater-Containing Silicate Corrosion Inhibitor.

The average biofilm thicknesses from three biofilms are shown in Figure 3a. The 6 month silicate biofilms (227 ± 43 μm) were significantly thicker than the 1 year groundwater biofilms (129 ± 29 μm), followed by the 6 month tin biofilms (126 ± 19 μm) based on KS test ($p < 0.05$). The biofilm thickness normalized by the growth period is shown in Figure 3a. The silicate biofilms developed the most among the three biofilms with a mean normalized thickness of 38 ± 7.1 μm/month, followed by the tin biofilms with a mean normalized thickness of 21 ± 3.2 μm/month. The groundwater biofilms without the corrosion inhibitor additions developed the least with a mean normalized thickness of 11 ± 2.4 μm/month. Previous studies suggested that the silicate-based corrosion inhibitors can prevent the leaching of metal ions into the drinking water by forming a protection layer on the pipe surface.[12,49,50] This protective layer formed on the pipe surface can increase the surface area and thus can aid in the cell adhesion and biofilm development.[17,51] Also, silicate biofilms were the most porous with a mean overall porosity of 0.17 ± 0.04. This porosity is larger than that of the groundwater biofilms without corrosion inhibitor with a mean overall porosity of 0.13 ± 0.05 and tin biofilms with a mean overall porosity of 0.11 ± 0.05 (t-test, $p < 0.05$) (Figure 3b). No significant difference was observed in porosities between the tin and groundwater biofilms (t-test, $p > 0.05$). In summary, when silicate was used as a corrosion inhibitor, biofilm grown from this amended water was thicker and more porous compared to biofilm grown from groundwater or groundwater-containing tin.

More Large Pores and Throats Were Detected for Silicate Biofilms Compared to Those for Tin Biofilms.

The effect of the structure of the pore space in the biofilms, in addition to the overall porosity, was studied by conducting pore network modeling (PNM) based on the OCT images obtained from the three biofilms. In a PNM, the pore space was represented by a series of spherical pores connected by cylindrical throats. Based on the PNM results, we obtained the number of pores and throats and their corresponding size distributions (Figure 4). The absolute pore throat number found in silicate biofilms was the greatest compared to that in tin and groundwater biofilms. However, silicate biofilms also had the greatest biofilm volume because of the greatest thickness compared to other biofilms. Thus, when we normalized the number of pores and throats of biofilms with the respective biofilm volume, the normalized numbers of pores of these three biofilms were not significantly different (ANOVA, $p > 0.05$). The numbers of pores per 10^6 μm^3 had a median value of 8.2 (95% confidence interval (CI): 3.9–8.7), 5.7 (95% CI: 2.0–11), and 6.2 (95% CI: 4.1–12) for the

silicate, tin, and groundwater biofilms, respectively. Despite the similar number of pores detected in three biofilms, the silicate biofilms had significantly more throats than the tin biofilms (KS test, $p < 0.05$). The numbers of throats per 10^7 μm^3 had a median value of 8.2 (95% CI: 3.9–13), 4.6 (95% CI: 1.5–6.3), and 6.4 (95% CI: 3.5–11) for the silicate, tin, and groundwater biofilms, respectively.

Because the axial resolution of OCT was around 5–8 μm, we only include the pores and throats with an equivalent radius above 5 μm in our following statistical analysis. The distributions of the pore equivalent radius determined by the PNM for these three biofilms are shown in Figure 5. Among the three studied biofilms, the distribution of the pore equivalent radius was significantly greater in the groundwater biofilms than those in the silicate and tin biofilms ($p < 0.05$). The median of the pore equivalent radius determined from silicate, tin, and groundwater biofilms is 7.0 (95% CI: 5.6–58 μm), 6.9 (95% CI: 5.5–55 μm), and 7.4 (95% CI: 5.1–59 μm), respectively. About 2 times more pores with an equivalent radius greater than 100 μm were found in silicate biofilms compared to those in groundwater biofilms. The median of the pore equivalent radius in groundwater biofilms was greater than that in silicate biofilms. However, more pores were found in silicate biofilms compared to groundwater biofilms in the greater pore equivalent radius range. The distribution of pore equivalent radius found in silicate biofilms was slightly but significantly greater than those in tin biofilms (KS test, $p < 0.05$). The distribution of the pore equivalent radius in the silicate biofilms showed about 11 times more pores with a radius greater than 100 μm compared to those in the tin biofilms.

The characteristics of throats connecting the pores are shown in Figure 6. The throat equivalent radius was greatest for silicate biofilms with a median of 17 μm (95% CI: 6.0–49 μm) compared to that in tin biofilms with a median of 15 μm (95% CI: 6.0–40 μm) and that for groundwater biofilms with a median of 15 μm (95% CI: 5.9–35 μm) (KS test, $p < 0.05$). A higher frequency of throats with a larger equivalent radius was detected for silicate biofilms compared to that for tin and groundwater biofilms. The throat length in silicate biofilms with a median of 193 μm (95% CI: 78–450 μm) was slightly greater compared to those in the tin biofilms with a median of 185 μm (95% CI: 82–416 μm). The distributions of the throat equivalent radius and length showed that more throats in the silicate biofilms had greater and longer connecting throats compared to those found in the other biofilms. About 6 and 24 times more throats with an equivalent radius greater than 65 μm were found in the silicate biofilms than those in the groundwater biofilms and the tin biofilms, respectively. Also, the number of throats in the silicate biofilms with length greater than 700 μm was about 7 and 5 times more than those in the tin and groundwater biofilms, respectively. More throats connecting the pores instead of isolated pores were also found in the silicate biofilms. Note that silicate biofilms also had a greater overall porosity compared to tin and groundwater biofilms. This greater overall porosity in silicate biofilms can be attributed to the higher detection frequency of larger connections and pore detections. Based on the pore network analysis results of the three biofilms, biofilms developed without corrosion inhibitors had the largest pore but smallest throats among the three biofilms (see the Table of Content art).

DISCUSSION

Biofilm detachment has been found to relate to biofilm stiffness.[24,26] A wide range of biofilm stiffness (10–10^8 Pa) was reported from single- and multispecies biofilms grown on various surfaces.[29-31] It is important to understand how biofilm stiffness can be attributed to the biofilm architecture, chemical composition, and growing conditions. For example, the elastic moduli of two strains of *Pseudomonas aeruginosa* biofilms grown for 3 days were in the range of 15–170 kPa.[39] These values were greater than those for silicate and groundwater biofilms but overlapped with tin biofilms. Microcolonies of *P. aeruginosa* developed in 3 days had the elastic modulus below 80 Pa.[52] These stiffness values were much lower than those of the three biofilms in this study, suggesting that young monospecies biofilms of *P. aeruginosa* were less stiff than the mature multispecies biofilms grown from low-nutrient drinking water. Biofilms grown from the same groundwater source in a similar CDC reactor setup had the elastic moduli in the range of 0–14 kPa.[24] This range overlapped with the elastic moduli of silicate and groundwater biofilms and half of those of tin biofilms. The greater stiffness in tin biofilms showed that using tin corrosion inhibitors can promote a biofilm that have more resistance to physical stress compared to that in silicate biofilms. The results of this study and our previous study using simulated drinking water suggest that drinking water biofilm stiffness may not be inferred from monospecies biofilms grown over a short time from nutrient-rich conditions.

We showed here that biofilm porous structure and development could adapt to the water chemical composition, which is altered by adding a corrosion inhibitor. We found that the addition of tin or silicate to groundwater led to faster biofilm growth rate on the PVC surface compared to biofilms developed with only groundwater. This faster development of silicate or tin biofilms can be caused by the formation of silicate or tin scales on the PVC surface that increased the surface area for cell adhesion and accumulation. Silicate scale formation on the pipe surface has been reported when silicate was used as a corrosion inhibitor.[13,49,50] The greater porosity observed with the thicker silicate biofilms can also be explained by the less resistance of nutrients transported through the bulk biofilms.[18] Significant thicker biofilms with polyphosphate were observed compared to groundwater biofilms, while thin biofilms developed under soft groundwater.[25] Minerals of calcium carbonate, such as calcite and aragonite, in untreated groundwater biofilms can result in a compact structure and a stiffer matrix compared to polyphosphate and soft groundwater biofilms.[25] The observation of faster biofilm development in the presence of tin or silicate compared to that fed by only groundwater demonstrated that although two nonphosphate corrosion inhibitors were not considered nutrient for bacteria, their presence can still promote biofilm growth. Pore structure was reported to be correlated with mechanical properties, such as stiffness and compress yield stress, in an engineered porous material.[35] The effective Young's modulus reduced with increasing porosity in ceramics.[53] However, the characterization of both biofilm stiffness and pore structure has not been conducted. Our results revealed that the abundant long or large water-filled connecting throats can contribute to the reduction of force measured during indentation into silicate biofilms under water. The results of this study showed that the presence of silicate and tin as corrosion inhibitors influenced the biofilm structure and stiffness. The biofilms developed under silicate corrosion inhibitor

were porous and soft, while those developed under tin corrosion inhibitor were compact and stiff. The stiffer tin biofilms can be more resistant to the shear stress induced by the water flow, and less detachment can be expected from tin biofilms compared to softer silicate biofilms.[25,26] Also, silicate biofilms can be expected to detach more due to their greatest thickness and fastest development among the three studied biofilms.

Silicate has been commonly used as a corrosion inhibitor in drinking water systems in the United States since 1920s.[13] Silicate may mitigate iron and manganese release through a colloidal dispersion mechanism. The exact mechanism of silicate for lead and copper corrosion control is still uncertain, and previous work suggested that silicate may reduce lead and copper release by increasing pH and/or formation of a protective layer on the pipe scales.[14] Tin (Sn)-based corrosion inhibitors are relatively new, and their exact role for corrosion control is still under investigation. Previous research suggested that Sn(II) may be oxidized to Sn(VI), which would mitigate lead release through the formation of low-solubility lead precipitates.[36] We also obtained the chemical composition of the studied biofilms using Fourier transform infrared spectroscopy (FTIR) and scanning electron microscopy (SEM) coupled with energy-dispersive X-ray spectroscopy (EDS). However, we did not get quantitative results that give a clear picture of the chemical composition of the studied biofilms because the signals of other components are much higher than those from silicate or tin.

Due to the complexity and heterogeneity of the biofilm development on the coupons, we cannot accurately determine the biofilm stiffness in the shear direction in this study. However, the near-surface stiffness measured by the indentations can also demonstrate the resistance to detachment by the shear flow.[24,25] The possible biomass detachment by the shear flow for these biofilms and the biofilm microbial composition should be quantified in future studies.

ENVIRONMENTAL RELEVANCE

Biofilm development and detachment can cause deterioration of drinking water esthetics (taste, odor, and discoloration), which was in about 80% of the consumer complaints received by the utilities.[9,54] In addition, consumers can be exposed to opportunistic pathogens in the water when biofilms detach by the water shear stress. About US$430 million and US$425 million of economic costs were estimated for the treatment of infection by the two most common opportunistic pathogens in drinking water, *Legionella* and nontuberculous *Mycobacteria* in the United States, respectively.[55] Because these two pathogens have been found in drinking water biofilms,[56-58] knowledge on how to control biofilm detachment could help to improve water quality at the taps. This study is the first to characterize the pore structure and the stiffness of biofilms grown from the groundwater, a source for drinking water, with or without a nonphosphate corrosion inhibitor. Silicate biofilms were thicker with a network of connecting pores, while tin biofilms were thinner with more isolated pores. The water-filled connected pores in silicate biofilms can contribute to the lower stiffness measurements by indentations. Previously, under stress applied by water flow, biofilms with lower stiffness tend to detach more compared to stiffer biofilms.

[24,26] The results of this study suggest that using tin instead of silicate as a corrosion inhibitor can potentially reduce biofilm growth and subsequent detachment in the DWDS.

Supplementary Material

Refer to Web version on PubMed Central for supplementary material.

ACKNOWLEDGMENTS

The authors acknowledge partial support from the Zhejiang–Illinois Institute and NSF Grant 1855609, and the National Institutes of Health Grant R01EB013723. The authors thank Dr. Guillermo L. Monroy from the University of Illinois at Urbana-Champaign for obtaining the OCT images. The authors thank the MATLAB code developed in Dr. Nicolas Derlon and Professor Eberhard Morgenroth from the Swiss Federal Institute of Aquatic Science and Technology (Eawag).

REFERENCES

(1). Hong P-Y; Hwang C; Ling F; Andersen GL; LeChevallier MW; Liu W-T Pyrosequencing Analysis of Bacterial Biofilm Communities in Water Meters of a Drinking Water Distribution System. Appl. Environ. Microbiol 2010, 76, 5631–5635. [PubMed: 20581188]

(2). Douterelo I; Husband S; Loza V; Boxall J Dynamics of Biofilm Regrowth in Drinking Water Distribution Systems. Appl. Environ. Microbiol 2016, 82, 4155–4168. [PubMed: 27208119]

(3). Douterelo I; Jackson M; Solomon C; Boxall J Microbial analysis of in situ biofilm formation in drinking water distribution systems: implications for monitoring and control of drinking water quality. Appl. Microbiol. Biotechnol 2016, 100, 3301–3311. [PubMed: 26637423]

(4). Cruz MC; Woo Y; Flemming H-C; Wuertz S Nitrifying niche differentiation in biofilms from full-scale chloraminated drinking water distribution system. Water Res. 2020, 176, No. 115738. [PubMed: 32259683]

(5). Hallam NB; West JR; Forster CF; Simms J The potential for biofilm growth in water distribution systems. Water Res. 2001, 35, 4063–4071. [PubMed: 11791835]

(6). Declerck P Biofilms: The environmental playground of Legionella pneumophila. Environ. Microbiol 2010, 12, 557–566. [PubMed: 19678829]

(7). Beer KD; Gargano JW; Roberts VA; Hill VR; Garrison LE; Kutty PK; Hilborn ED; Wade TJ; Fullerton KE; Yoder JS Surveillance for waterborne disease outbreaks associated with drinking water—United States, 2011–2012. MMWR, Morb. Mortal Wkly. Rep 2015, 64, 842–848. [PubMed: 26270059]

(8). Wang H; Masters S; Hong Y; Stallings J; Falkinham JO; Edwards MA; Pruden A Effect of Disinfectant, Water Age, and Pipe Material on Occurrence and Persistence of Legionella, mycobacteria, *Pseudomonas aeruginosa*, and Two Amoebas. Environ. Sci. Technol 2012, 46, 11566–11574. [PubMed: 23046164]

(9). Prest EI; Hammes F; van Loosdrecht MCM; Vrouwenvelder JS Biological Stability of Drinking Water: Controlling Factors, Methods, and Challenges. Front. Microbiol 2016, 7, No. 45. [PubMed: 26870010]

(10). LeChevallier MW; Schulz W; Lee RG Bacterial nutrients in drinking water. Appl. Environ. Microbiol 1991, 57, 857–862. [PubMed: 2039235]

(11). Liu S; Gunawan C; Barraud N; Rice SA; Harry EJ; Amal R Understanding, Monitoring, and Controlling Biofilm Growth in Drinking Water Distribution Systems. Environ. Sci. Technol 2016, 50, 8954–8976. [PubMed: 27479445]

(12). Hosseinibalajadeh S Lead Corrosion Inhibitors in Drinking Water; The University of Wisconsin: Milwaukee, 2018.

(13). Thompson JL; Scheetz BE; Schock MR; Lytle DA; Delaney PJ In *Sodium Silicate Corrosion Inhibitors: Issues of Effectiveness and Mechanism*, Water Quality Technology Conference; American Water Works Association, 1997.

(14). Schock MR; Lytle DA; Sandvig AM; Clement J; Harmon SM Replacing polyphosphate with silicate to solve lead, copper, and source water iron problems. J. Am. Water Works Assoc 2005, 97, 84–93.

(15). Hozalski RM; Ying T; Dai X Investigation of Stannous Chloride as an Inhibitor of Lead Corrosion; Water Research Foundation, 2010.

(16). Neu L; Proctor CR; Walser J-C; Hammes F Small-Scale Heterogeneity in Drinking Water Biofilms. Front. Microbiol 2019, 10, No. 2446. [PubMed: 31736893]

(17). Shen Y; Monroy GL; Derlon N; Janjaroen D; Huang C; Morgenroth E; Boppart SA; Ashbolt NJ; Liu W-T; Nguyen TH Role of Biofilm Roughness and Hydrodynamic Conditions in *Legionella pneumophila* Adhesion to and Detachment from Simulated Drinking Water Biofilms. Environ. Sci. Technol 2015, 49, 4274–4282. [PubMed: 25699403]

(18). Fortunato L; Qamar A; Wang Y; Jeong S; Leiknes T In-situ assessment of biofilm formation in submerged membrane system using optical coherence tomography and computational fluid dynamics. J. Membr. Sci 2017, 521, 84–94.

(19). Xi C; Marks D; Schlachter S; Luo W; Boppart SA High-resolution three-dimensional imaging of biofilm development using optical coherence tomography. J. Biomed. Opt 2006, 11, No. 034001.

(20). Hou J; Wang C; Rozenbaum RT; Gusnaniar N; de Jong ED; Woudstra W; Geertsema-Doornbusch GI; Atema-Smit J; Sjollema J; Ren Y; Busscher HJ; van der Mei HC Bacterial Density and Biofilm Structure Determined by Optical Coherence Tomography. Sci. Rep 2019, 9, No. 9794. [PubMed: 31278369]

(21). Walters MC 3rd; Roe F; Bugnicourt A; Franklin MJ; Stewart PS Contributions of antibiotic penetration, oxygen limitation, and low metabolic activity to tolerance of *Pseudomonas aeruginosa* biofilms to ciprofloxacin and tobramycin. Antimicrob. Agents Chemother 2003, 47, 317–323. [PubMed: 12499208]

(22). Nerenberg R The membrane-biofilm reactor (MBfR) as a counter-diffusional biofilm process. Curr. Opin. Biotechnol 2016, 38, 131–136. [PubMed: 26874609]

(23). Reichhardt C; Parsek MR Confocal Laser Scanning Microscopy for Analysis of *Pseudomonas aeruginosa* Biofilm Architecture and Matrix Localization. Front. Microbiol 2019, 10, No. 677. [PubMed: 31001240]

(24). Shen Y; Huang C; Monroy GL; Janjaroen D; Derlon N; Lin J; Espinosa-Marzal R; Morgenroth E; Boppart SA; Ashbolt NJ; Liu W-T; Nguyen TH Response of Simulated Drinking Water Biofilm Mechanical and Structural Properties to Long-Term Disinfectant Exposure. Environ. Sci. Technol 2016, 50, 1779–1787. [PubMed: 26756120]

(25). Shen Y; Huang PC; Huang C; Sun P; Monroy GL; Wu W; Lin J; Espinosa-Marzal RM; Boppart SA; Liu W-T; Nguyen TH Effect of divalent ions and a polyphosphate on composition, structure, and stiffness of simulated drinking water biofilms. npj Biofilms Microbiomes 2018, 4, No. 15. [PubMed: 30038792]

(26). Shen Y; Huang C; Lin J; Wu W; Ashbolt NJ; Liu W-T; Nguyen TH Effect of disinfectant exposure on *Legionella pneumophila* associated with simulated drinking water biofilms: release, inactivation, and infectivity. Environ. Sci. Technol 2017, 51, 2087–2095. [PubMed: 28085262]

(27). Tierra G; Pavissich JP; Nerenberg R; Xu Z; Alber MS Multicomponent model of deformation and detachment of a biofilm under fluid flow. J. R. Soc. Interface 2015, 12, No. 45.

(28). Abe Y; Polyakov P; Skali-Lami S; Francius G Elasticity and physico-chemical properties during drinking water biofilm formation. Biofouling 2011, 27, 739–750. [PubMed: 21762041]

(29). Peterson BW; He Y; Ren Y; Zerdoum A; Libera MR; Sharma PK; van Winkelhoff A-J; Neut D; Stoodley P; van der Mei HC; Busscher HJ Viscoelasticity of biofilms and their recalcitrance to mechanical and chemical challenges. FEMS Microbiol. Rev 2015, 39, 234–245. [PubMed: 25725015]

(30). Zeng G; Vad BS; Dueholm MS; Christiansen G; Nilsson M; Tolker-Nielsen T; Nielsen PH; Meyer RL; Otzen DE Functional bacterial amyloid increases Pseudomonas biofilm hydrophobicity and stiffness. Front. Microbiol 2015, 6, No. 1099. [PubMed: 26500638]

(31). Shaw T; Winston M; Rupp CJ; Klapper I; Stoodley P Commonality of Elastic Relaxation Times in Biofilms. Phys. Rev. Lett 2004, 93, No. 098102. [PubMed: 15447143]

(32). Fish K; Osborn AM; Boxall JB Biofilm structures (EPS and bacterial communities) in drinking water distribution systems are conditioned by hydraulics and influence discolouration. Sci. Total Environ 2017, 593–594, 571–580.

(33). Sanz-Herrera JA; García-Aznar JM; Doblaré M On scaffold designing for bone regeneration: A computational multiscale approach. Acta Biomater. 2009, 5, 219–229. [PubMed: 18725187]

(34). Lin CY; Kikuchi N; Hollister SJ A novel method for biomaterial scaffold internal architecture design to match bone elastic properties with desired porosity. J. Biomech 2004, 37, 623–636. [PubMed: 15046991]

(35). Torres-Sanchez C; Al Mushref FRA; Norrito M; Yendall K; Liu Y; Conway PP The effect of pore size and porosity on mechanical properties and biological response of porous titanium scaffolds. Mater. Sci. Eng., C 2017, 77, 219–228.

(36). Hozalski RM; Esbri-Amador E; Chen CF Comparison of stannous chloride and phosphate for lead corrosion control. J. Am. Water Works Assoc 2005, 97, 89–103.

(37). Baniasadi M; Xu Z; Gandee L; Du Y; Lu H; Zimmern P; Minary M Nanoindentation of *Pseudomonas aeruginosa* bacterial biofilm using atomic force microscopy. Mater. Res. Express 2014, 1, No. 045411.

(38). Andrews JW; Bowen J; Cheneler D Optimised determination of viscoelastic properties using compliant measurement systems. Soft Matter 2013, 9, 5581–5593.

(39). Lau PCY; Dutcher JR; Beveridge TJ; Lam JS Absolute Quantitation of Bacterial Biofilm Adhesion and Viscoelasticity by Microbead Force Spectroscopy. Biophys. J 2009, 96, 2935–2948. [PubMed: 19348775]

(40). Thomas G; Burnham NA; Camesano TA; Wen Q Measuring the Mechanical Properties of Living Cells Using Atomic Force Microscopy. J. Vis. Exp 2013, 76, No. 50497.

(41). Lee J-J; Rao S; Kaushik G; Azeloglu EU; Costa KD Dehomogenized Elastic Properties of Heterogeneous Layered Materials in AFM Indentation Experiments. Biophys. J 2018, 114, 2717–2731. [PubMed: 29874620]

(42). Huang P; Chaney EJ; Shelton RL; Boppart SA Magnetomotive Displacement of the Tympanic Membrane Using Magnetic Nanoparticles: Toward Enhancement of Sound Perception. IEEE Trans. Biomed. Eng 2018, 65, 2837–2846. [PubMed: 29993404]

(43). Schindelin J; Arganda-Carreras I; Frise E; Kaynig V; Longair M; Pietzsch T; Preibisch S; Rueden C; Saalfeld S; Schmid B; Tinevez J-Y; White DJ; Hartenstein V; Eliceiri K; Tomancak P; Cardona A Fiji: an open-source platform for biological-image analysis. Nat. Methods 2012, 9, 676–682. [PubMed: 22743772]

(44). Derlon N; Peter-Varbanets M; Scheidegger A; Pronk W; Morgenroth E Predation influences the structure of biofilm developed on ultrafiltration membranes. Water Res. 2012, 46, 3323–3333. [PubMed: 22534121]

(45). Gerke KM; Vasilyev RV; Khirevich S; Collins D; Karsanina MV; Sizonenko TO; Korost DV; Lamontagne S; Mallants D Finite-difference method Stokes solver (FDMSS) for 3D pore geometries: Software development, validation and case studies. Comput. Geosci 2018, 114, 41–58.

(46). Carrel M; Morales VL; Beltran MA; Derlon N; Kaufmann R; Morgenroth E; Holzner M Biofilms in 3D porous media: Delineating the influence of the pore network geometry, flow and mass transfer on biofilm development. Water Res. 2018, 134, 280–291. [PubMed: 29433078]

(47). Sekhon JS Multivariate and Propensity Score Matching Software with Automated Balance Optimization: The Matching Package for R. J. Stat. Software 2011, 42, No. 52.

(48). Lieleg O; Caldara M; Baumgartel R; Ribbeck K Mechanical robustness of Pseudomonas aeruginosa biofilms. Soft Matter 2011, 7, 3307–3314. [PubMed: 21760831]

(49). Rushing JC; McNeill LS; Edwards M Some effects of aqueous silica on the corrosion of iron. Water Res. 2003, 37, 1080–1090. [PubMed: 12553983]

(50). Gao H; Li Q; Chen FN; Dai Y; Luo F; Li LQ Study of the corrosion inhibition effect of sodium silicate on AZ91D magnesium alloy. Corros. Sci 2011, 53, 1401–1407.

(51). Ammar Y; Swailes D; Bridgens B; Chen J Influence of surface roughness on the initial formation of biofilm. Surf. Coat. Technol 2015, 284, 410–416.

(52). Kundukad B; Seviour T; Liang Y; Rice SA; Kjelleberg S; Doyle PS Mechanical properties of the superficial biofilm layer determine the architecture of biofilms. Soft Matter 2016, 12, 5718–5726. [PubMed: 27273453]

(53). Savchenko N; Sevostyanova I; Sablina T; Gömze L; Kulkov S The influence of porosity on the elasticity and strength of alumina and zirconia ceramics. AIP Conf. Proc 2014, 1623, 547–550.

(54). Vreeburg JHG; Boxall JB Discolouration in potable water distribution systems: A review. Water Res. 2007, 41, 519–529. [PubMed: 17174377]

(55). Falkinham JO; Pruden A; Edwards M Opportunistic Premise Plumbing Pathogens: Increasingly Important Pathogens in Drinking Water. Pathogens 2015, 4, 373–386. [PubMed: 26066311]

(56). Feazel LM; Baumgartner LK; Peterson KL; Frank DN; Harris JK; Pace NR Opportunistic pathogens enriched in showerhead biofilms. Proc. Natl. Acad. Sci. U.S.A 2009, 106, 16393–16399. [PubMed: 19805310]

(57). Lehtola MJ; Torvinen E; Kusnetsov J; Pitkänen T; Maunula L; von Bonsdorff C-H; Martikainen PJ; Wilks SA; Keevil CW; Miettinen IT Survival of *Mycobacterium avium, Legionella pneumophila, Escherichia coli*, and Caliciviruses in Drinking Water-Associated Biofilms Grown under High-Shear Turbulent Flow. Appl. Environ. Microbiol 2007, 73, 2854–2859. [PubMed: 17337541]

(58). Wang H; Edwards M; Falkinham JO; Pruden A Molecular Survey of the Occurrence of Legionella spp., Mycobacterium spp., *Pseudomonas aeruginosa*, and Amoeba Hosts in Two Chloraminated Drinking Water Distribution Systems. Appl. Environ. Microbiol 2012, 78, 6285–6294. [PubMed: 22752174]

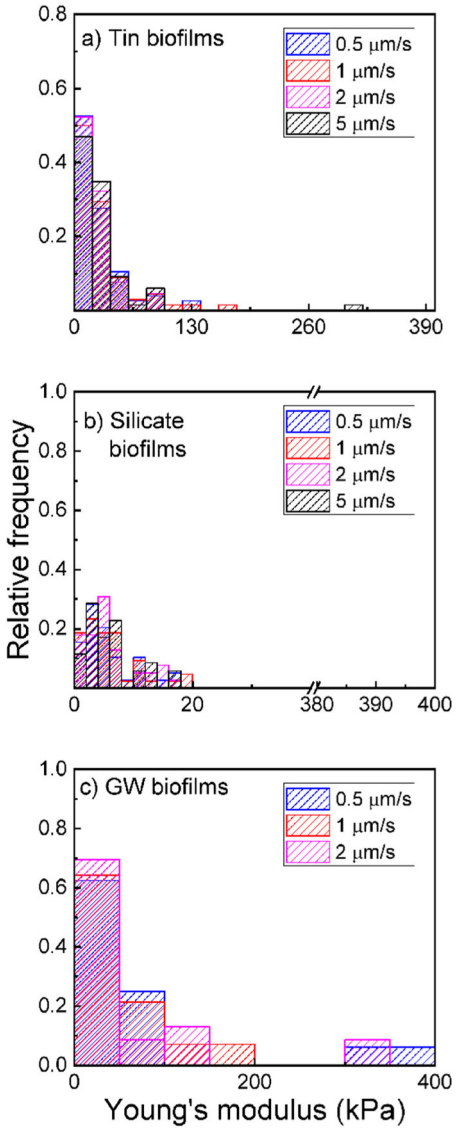

Figure 1.

Relative frequency of the measured Young's modulus from (a) tin biofilms, (b) silicate biofilms, and (c) groundwater (GW) biofilms.

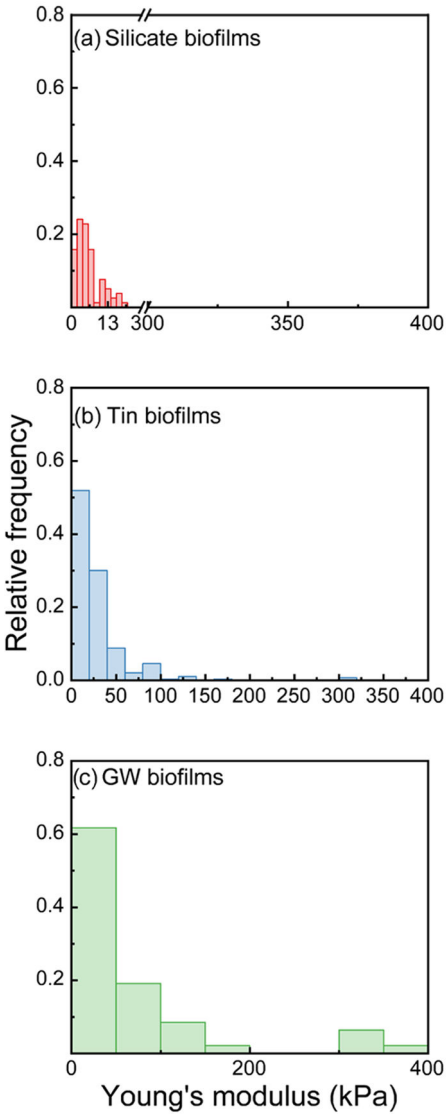

Figure 2.

Total relative frequency of the measured Young's modulus from three biofilms: silicate biofilms (a, red), tin biofilms (b, blue), and groundwater biofilms (c, green).

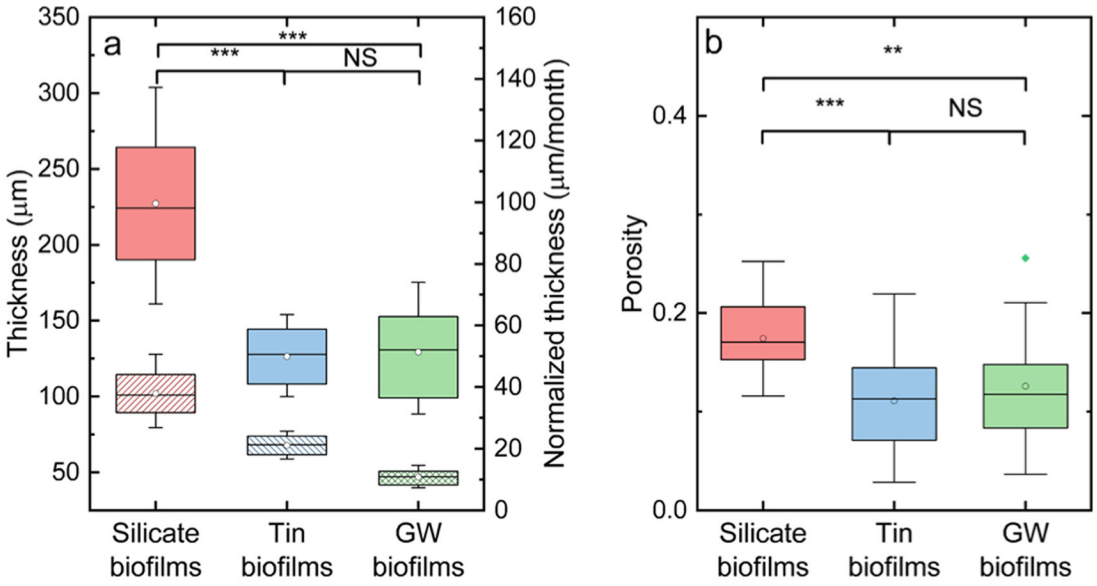

Figure 3.

(a) Thickness (solid) and normalized thickness (pattern) of silicate, tin, and groundwater biofilms. (b) Overall porosities of silicate, tin, and groundwater biofilms. The diamond dots indicate the means. The straight lines indicate the median, and the bounds of the colored boxes indicate 25–75th percentiles of the distributions. The asterisk indicates that there was a significant difference between two groups of data, as found with (a) the Wilcoxon rank-sum test and (b) KS hypothesis test. Two asterisks indicated a *p*-value less than 0.01 while three asterisks indicated a *p*-value less than 0.001. NS indicated that no significant difference was detected.

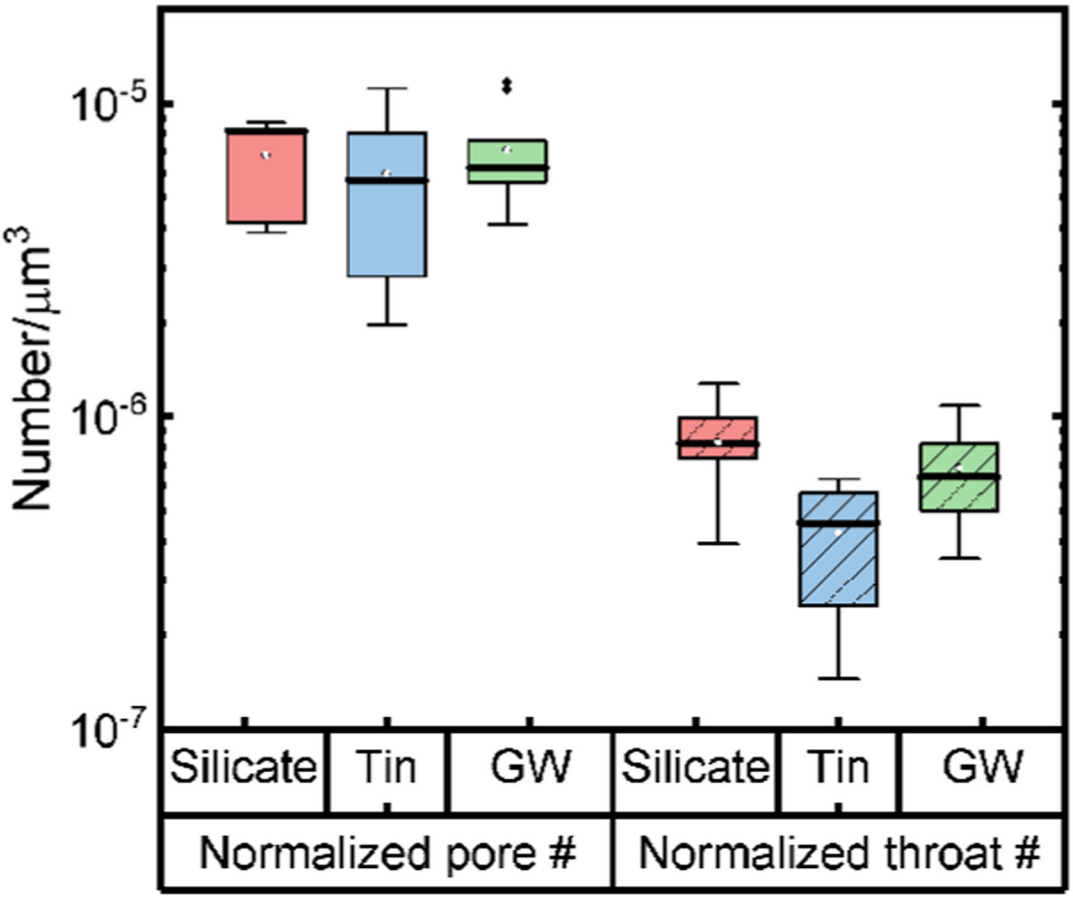

Figure 4.

Normalized pore (solid) and throat (dashed) numbers by the biofilm volume of silicate (red), tin (blue), and groundwater (green) biofilms. Points outside of the tail indicate outliers of the data obtained for groundwater (GW) biofilms. This outlier was not observed for other biofilms.

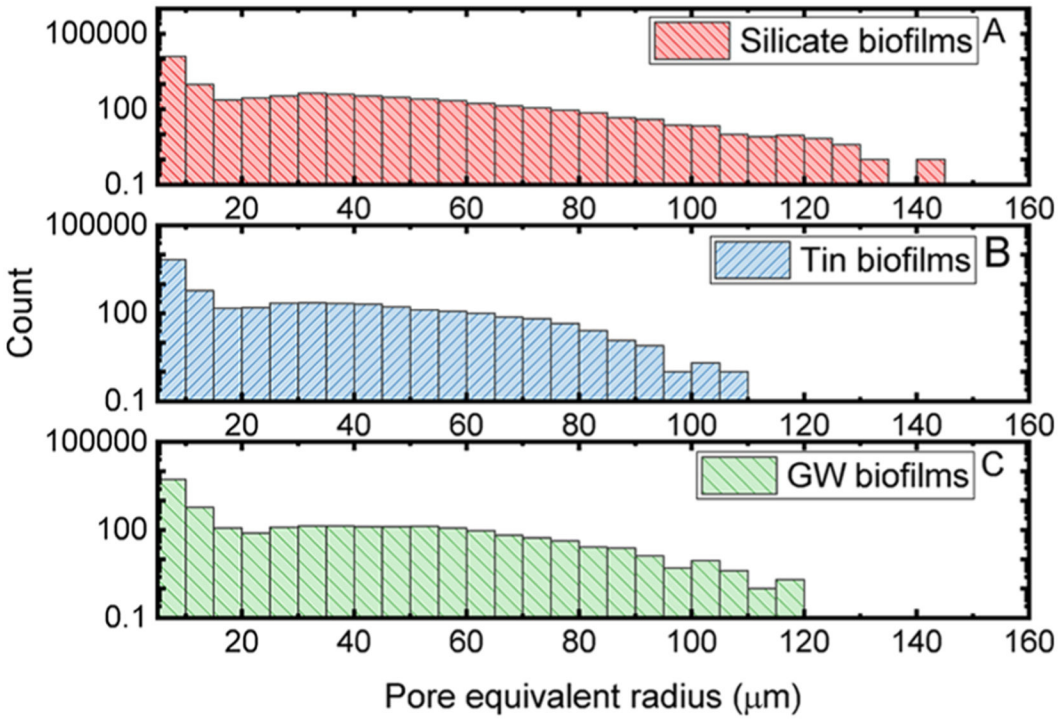

Figure 5.
Distributions of pore equivalent radius in silicate (A, red), tin (B, blue), and groundwater (C, green) biofilms.

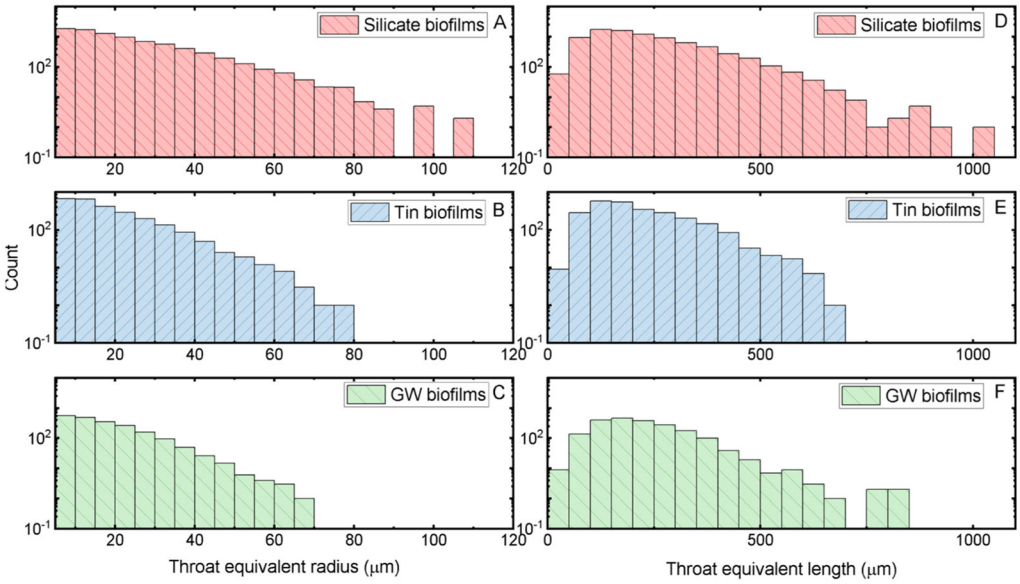

Figure 6.

Throat equivalent radius (A–C) and length (D–F) from silicate biofilms (red), tin biofilms (blue), and groundwater biofilms (green).